

International Journal of Modern Physics D  
 © World Scientific Publishing Company

## Recurrence Analysis as a tool to study chaotic dynamics of extreme mass ratio inspiral in signal with noise

Georgios Lukes-Gerakopoulos

*Astronomical Institute of the Academy of Sciences of the Czech Republic, Boční II 1401/1a,  
 CZ-141 31 Prague, Czech Republic  
 gglukes@gmail.com*

Ondřej Kopáček

*Astronomical Institute of the Academy of Sciences of the Czech Republic, Boční II 1401/1a,  
 CZ-141 31 Prague, Czech Republic  
 kopacek@ig.cas.cz*

Received Day Month Year

Revised Day Month Year

Recurrence analysis is a well settled method allowing to discern chaos from order, and determinism from noise. We apply this tool to study time series representing geodesic and inspiraling motion of a test particle in a deformed Kerr spacetime, when deterministic chaos and different levels of stochastic noise are present. In particular, we suggest a recurrence-based criterion to reveal whether the time series comes from a deterministic source and find a noise-level threshold of its applicability.

*Keywords:* black holes;chaos

04.25.dg; 04.70.Bw; 95.10.Fh

### 1. Introduction

Extreme mass ratio inspirals (EMRIs) are highly promising sources of gravitational waves for detectors like the Laser Interferometer Space Antenna (LISA).<sup>1</sup> To form an EMRI, a stellar compact object, e.g., a black hole or a neutron star, has to be trapped in the gravitational field of a supermassive black hole (SMBH). As the stellar compact object is orbiting the SMBH, gravitational waves are emitted forcing the stellar object to follow an inspiraling trajectory. To detect these gravitational waves, template banks are built in order to use them for the matched filtering method. For constructing these templates it is assumed that the spacetime background is described by the Kerr metric and that the inspiraling compact object shifts adiabatically from a geodesic orbit to a geodesic orbit.<sup>2</sup> The above standard *adiabatic approximation* implies that the geodesic orbits are regular since Kerr spacetime corresponds to an integrable system. If the system is not integrable, then non-linear phenomena like chaos and prolonged resonances will appear.<sup>3,4</sup> However,

2 *Georgios Lukes-Gerakopoulos, Ondřej Kopáček*

the current template banks do not include such scenarios, which means that in such cases matched filtering would fail.

In fact, the standard adiabatic approximation neglects various factors leading to non-integrability. For example, if the spin of the inspiraling object is taken into account then chaotic motion appears;<sup>5–8</sup> the presence of an outer stellar object orbiting around an EMRI can cause “butterfly” effects to the inspiraling object;<sup>9</sup> the presence of a matter distribution, like a halo or a ring, around a black hole acts as a source of chaos.<sup>10–15</sup> In the above cases the Kerr black hole hypothesis<sup>16</sup> is assumed to hold for the SMBH. However, it has been shown that spacetimes diverging from the Kerr by a deformation parameter can also result in non-integrable systems.<sup>4, 17–19</sup> The apparent question is how different would be the gravitational waveforms coming from chaotic orbits compared with those coming from regular ones.

To address this question the emitted gravitational radiation of spinning objects in a Kerr background was studied by Kiuchi and Maeda.<sup>3</sup> First they investigated whether the waveforms resulting from a regular and a chaotic orbit bear any significant differences and they found that the respective waveforms look similar. Then they applied a Fourier transform on the waveforms to obtain the corresponding energy spectra. In the case of a chaotic orbit they found a continuous spectrum with several peaks, while for a regular orbit the spectrum was discrete. This is a basic method to distinguish between chaotic and regular orbits in a conservative system, see, e.g., Ref. 20. However, in an actual EMRI the dissipation due to the radiation reaction is always present and the inspiraling object is losing energy and angular momentum. By including the dissipation factor, the peaks of the spectrum shift, since the trajectory itself shifts from an orbit to an orbit. The result of such a shift is that for a regular orbit one does not necessarily obtain a discrete spectrum anymore and in this sense the spectra of the regular and the chaotic orbit become similar. In fact, for weak chaos in conservative systems, such shifts of peaks are used as an indicator to show that an orbit is chaotic.<sup>21</sup> The problem of detecting gravitational waves coming from potentially chaotic orbits is even more complicated since the received waveforms are expected to be buried in various types of noise.<sup>1</sup> Thus, the Fourier spectrum of a real signal is always contaminated by noise and the identification of the deterministic signal becomes intricate even for the conservative systems.

Since the existing template banks do not include scenarios where non-linear phenomena are present in the dynamics of the source, the question is how one can distinguish noise from deterministic signal without selecting a particular model of an EMRI. Although, the current work does not answer the given question, it provides a study of a particular statistical method that is applied to simulated data from a dynamical system that is a simplified model of EMRI. Namely, we use a statistical analysis of recurrences occurring in time series produced by a body moving in Manko, Sanabria-Gómez, Manko (MSM) spacetime,<sup>22</sup> since MSM provides chaotic geodesic orbits,<sup>19, 23, 24</sup> to study up to which noise level geodesic chaos can

be detected even when dissipation is present. The MSM spacetime is an exact vacuum solution of the Einstein's field equations and describes the "exterior field of a charged, magnetized, spinning deformed mass".<sup>22</sup> The MSM spacetime serves in our analysis as an "easy" way to simulate a non-integrable EMRI system, and this choice does not restrict the generality of our analysis. This analysis could be applied with any of the above mentioned parameters inducing a non-integrable behavior of an EMRI, e.g., by including the spin of the particle just like Kiuchi and Maeda did.<sup>3</sup> This is something we actually plan to do once the gravitational wave fluxes from spinning particles are obtained, see, e.g., Ref. 25.

The rest of the article is organized as follows. In Sec. 2 the MSM spacetime is introduced. Sec. 3 discusses the Lyapunov number and the recurrence analysis. In Sec. 4 the recurrence analysis is applied on simulated data. At first we inspect the case of geodesic motion in a MSM spacetime with different noise levels, and then we also consider the generalized scenario including the dissipation due to radiation reaction. Sec. 5 concludes the paper. The appendix provides technical details about the parameters used in the recurrence analysis.

## 2. Spacetime background

The MSM metric was designed to model neutron stars,<sup>22,26,27</sup> but here we reduce it to a deformed Kerr spacetime which is known to trigger geodesic chaos.<sup>19,23</sup> The MSM spacetime depends on five real parameters describing this central object: the mass  $M$ , the spin  $a$  (per unit mass  $M$ ), the total charge  $q$ , the magnetic dipole moment  $\mathcal{M}$ , and the mass-quadrupole moment  $\mathcal{Q}$ . The latter two parameters are actually represented in the metric as functions of two other parameters  $b$  and  $\mu$ , i.e.

$$\mathcal{M} = \mu + q(a - b) \quad , \quad (1)$$

$$\mathcal{Q} = -M(d - \delta - a b + a^2) \quad , \quad (2)$$

where

$$\delta := \frac{\mu^2 - M^2 b^2}{M^2 - (a - b)^2 - q^2}, \quad d := \frac{1}{4}[M^2 - (a - b)^2 - q^2] \quad . \quad (3)$$

For the purpose of our work we set the charge  $q$  and the parameter  $\mu$  to zero, thus, the magnetic dipole moment (1) is set to zero. This also reduces the mass-quadrupole moment (2) to

$$\mathcal{Q} = -M \left( \frac{(M^2 - (a - b)^2)^2 + 4 M^2 b^2}{4(M^2 - (a - b)^2)} - a b + a^2 \right) \quad , \quad (4)$$

where  $b$  is now the only parameter making the MSM spacetime to deviate from a Kerr one. In particular, when  $b^2 = a^2 - M^2$  Eq. (4) gives  $\mathcal{Q}_{\text{Kerr}} = -aM^2$ , and the MSM spacetime reduces to Kerr. If we define the quadrupole deviation parameter

$$q := \mathcal{Q} - \mathcal{Q}_{\text{Kerr}} \quad , \quad (5)$$

4 *Georgios Lukes-Gerakopoulos, Ondřej Kopáček*

then for  $q > 0$  the MSM describes a more prolate compact object than the Kerr black hole and for  $q < 0$  a more oblate one, while for  $q = 0$  the MSM identifies with the Kerr black hole. Thus, in this sense MSM is a bumpy black hole, i.e., a compact object deviating from a Kerr black hole.<sup>4,16,18</sup> Such bumpy black holes are often employed to test the Kerr hypothesis in EMRIS.<sup>4,16,18</sup>

A line element in Weyl-Papapetrou coordinates reads

$$ds^2 = -f(dt - \omega d\phi)^2 + f^{-1} [e^{2\gamma}(d\rho^2 + dz^2) + \rho^2 d\phi^2] \quad . \quad (6)$$

For the MSM the metric functions read

$$f = \mathcal{E}/D, \quad e^{2\gamma} = \mathcal{E}/16\kappa^8(u^2 - v^2)^4, \quad \omega = (v^2 - 1)F/\mathcal{E} \quad , \quad (7)$$

where

$$\mathcal{E} := R^2 + \lambda_1\lambda_2S^2, \quad D := \mathcal{E} + RP + \lambda_2ST, \quad F := RT - \lambda_1SP \quad , \quad (8)$$

$$\lambda_1 := \kappa^2(u^2 - 1), \quad \lambda_2 := v^2 - 1 \quad , \quad (9)$$

and

$$\begin{aligned} P &:= 2\{\kappa Mu[(2\kappa u + M)^2 - 2v^2(2\delta + ab - b^2) \\ &\quad - a^2 + b^2 - q^2] - 2\kappa^2q^2u^2 - 2v^2(4\delta d - M^2b^2)\} \quad , \\ R &:= 4[\kappa^2(u^2 - 1) + \delta(1 - v^2)]^2 + (a - b)[(a - b)(d - \delta) - M^2b + q\mu](1 - v^2)^2 \quad , \\ S &:= -4(a - b)[\kappa^2(u^2 - v^2) + 2\delta v^2] + v^2(M^2b - q\mu) \quad , \\ T &:= 4(2\kappa Mb u + 2M^2b - q\mu)[\kappa^2(u^2 - 1) + \delta(1 - v^2)] + (1 - v^2)\{(a - b)(M^2b^2 - 4\delta d) \\ &\quad - (4\kappa Mu + 2M^2 - q^2)[(a - b)(d - \delta) - M^2b + q\mu]\} \quad . \end{aligned} \quad (10)$$

All the metric functions are expressed in prolate spheroidal coordinates  $u, v$ . However, the line element (6) is written in the corresponding cylindrical coordinates  $\rho, z$ . The transformation between these coordinate systems is given by

$$\rho = \kappa\sqrt{(u^2 - 1)(1 - v^2)}, \quad z = \kappa uv \quad , \quad (11)$$

where

$$\kappa := \sqrt{d + \delta} \quad . \quad (12)$$

### 2.1. Geodesic motion

The Lagrangian function

$$L = \frac{1}{2}g_{\mu\nu} \dot{x}^\mu \dot{x}^\nu \quad (13)$$

provides the equations of geodesic motion in a spacetime with metric  $g_{\mu\nu}$ . The dot denotes derivation with respect to proper time  $\tau$ , thus the Lagrangian (13) expresses the four-velocity  $g_{\mu\nu} \dot{x}^\mu \dot{x}^\nu = -1$  constraint.

Since the spacetime is stationary and axisymmetric, the specific energy

$$E = -\frac{\partial L}{\partial t} \quad , \quad (14)$$

and the specific azimuthal component of the angular momentum

$$L_z = \frac{\partial L}{\partial \dot{\phi}} \quad , \quad (15)$$

are conserved. For simplicity, we set  $M = 1$ , which is equivalent with replacing all the quantities with their dimensionless counterparts, e.g.,  $\tau/M$ ,  $\rho/M$ . Thus, we refer hereafter to the above two integrals of motion as the energy and the angular momentum.

Through Eqs. (14) and (15) we restrict the motion on the meridian plane. Thus, from the original set of 4 coupled second order ordinary differential equations, we arrive to a set of 2 coupled ODEs.

### 3. Chaos Detection

#### 3.1. Lyapunov number

A common way to distinguish between chaotic and regular orbits are indicators depending on the deviation vector  $\xi^\alpha$ . A deviation vector can be interpreted as an indicator of how two initially nearby worldlines  $x^\alpha$  and  $x^\alpha + \xi^\alpha$  diverge from each other. The evolution of the deviation vector along the geodesic orbit is provided by the geodesic deviation equation

$$\ddot{\xi}^\alpha + 2\Gamma_{\beta\gamma}^\alpha \dot{x}^\beta \dot{\xi}^\gamma + \frac{\partial \Gamma_{\beta\gamma}^\alpha}{\partial x^\delta} \dot{x}^\beta \dot{x}^\gamma \xi^\delta = 0 \quad . \quad (16)$$

However, a deviation vector in the classical framework should represent the phase space neighborhood around a point of the trajectory and not only the configuration space. A deviation vector should show how the phase space is stretched and folded in the neighborhood of the trajectory during the evolution. To address this, Sota et al. in Ref. 29 defined an invariant measure of the deviation vector as

$$\Xi^2 = g_{\alpha\beta} \xi^\alpha \xi^\beta + g_{\alpha\beta} \frac{D\xi^\alpha}{d\tau} \frac{D\xi^\beta}{d\tau} \quad , \quad (17)$$

where the covariant derivative

$$\frac{D\xi^\alpha}{d\tau} = \dot{\xi}^\alpha + \Gamma_{\beta\gamma}^\alpha \dot{x}^\beta \xi^\gamma \quad (18)$$

provides the divergence of the velocities.

For a regular orbit the measure of the deviation vector grows linearly, while for a chaotic one, it grows exponentially, see, e.g., Ref. 28. As an invariant measure of the evolution parameter the proper time normalized by the time scale  $GM/c^3$  was used in Ref. 29, which reduces to  $M$  in our case, as we employ geometric units ( $G = c = 1$ ).

6 *Georgios Lukes-Gerakopoulos, Ondřej Kopáček*

To measure chaos, usually the maximal Lyapunov Characteristic Exponent

$$\text{mLCE} = \frac{1}{\tau} \ln \frac{\Xi(\tau)}{\Xi(0)} \quad (19)$$

is utilized. Even if in theory the mLCE should be calculated for the  $\tau \rightarrow \infty$  limit, practically  $\tau$  has a large but finite value. Lyapunov numbers are a standard way to measure chaos, but they cannot distinguish chaos from noise. To address the latter issue we employ methods based on the statistical analysis of recurrences in a data time series, i.e., the recurrence plots and recurrence quantification analysis.<sup>30</sup>

### 3.2. Recurrence Analysis

The recurrence of a general (vector) time series  $\mathbf{y}(t)$  occurs when the distance (measured in an abstract phase space) between the  $i$ th point and the  $j$ th point of the data series drops below a pre-defined threshold  $\varepsilon$ . Recurrences are recorded in the (binary) recurrence matrix

$$\mathbf{R}_{ij}(\varepsilon) = \Theta(\varepsilon - \|\mathbf{y}(i) - \mathbf{y}(j)\|) \quad , \quad (20)$$

where  $\|\cdot\|$  is the norm, and  $\Theta$  stands for the Heaviside step-function. Recurrence matrix  $\mathbf{R}_{ij}$  may be visualized as a recurrence plot (RP).<sup>31</sup> Actually, RPs encode surprising amount of fundamental information about the dynamics of the trajectory.<sup>32</sup> Just a visual survey of RPs provides an intuitive method of how to discern regular from chaotic motion and deterministic signal from noise.<sup>33,34</sup> An optimal choice of the recurrence threshold  $\varepsilon$  is crucial for the reliable outcome of the analysis. Several rules of thumb have been suggested, e.g., to use the value of  $\varepsilon$  which corresponds to 10% of the mean phase space diameter, or 25% of the standard deviation of the analyzed data.<sup>35</sup> Nevertheless, for our application the optimal method is to set  $\varepsilon$  which ensures given recurrences point density (namely 2% in our case).

In order to show how deterministic motion can be discerned from noise by RP techniques we identify the different types of dynamics of geodesic orbits on a Poincaré section and provide the corresponding RP. In particular, the top left panel of Fig. 1 shows a Poincaré section on the plane  $(\rho, \dot{\rho})$  which includes the analyzed orbits. On this section the chaotic sea (scattered points) surrounds KAM curves (homocentric closed curves) forming the main island of stability. According to the method described in Sec. 3.1 the maximal Lyapunov number of the orbit belonging to the chaotic sea was found to be  $\text{mLCE} \simeq 10^{-2.87}$ . For numerical details of the calculation see Ref. 24.

Deterministic systems generally tend to produce characteristic linear patterns in a RP. Regular orbits typically form long diagonal lines, while deterministic chaos results in a more complex pattern, as shown in the bottom left and bottom right panels of Fig. 1 respectively. Noise produces almost homogeneously distributed recurrence points (top right panel of Fig. 1). Noise in this work is represented by the *Mathematica* function `RandomReal[-x, x]`, which gives a pseudorandom real number in the range  $[-x, x]$ , where  $x$  is a real positive number. The  $i, j$  axes on the

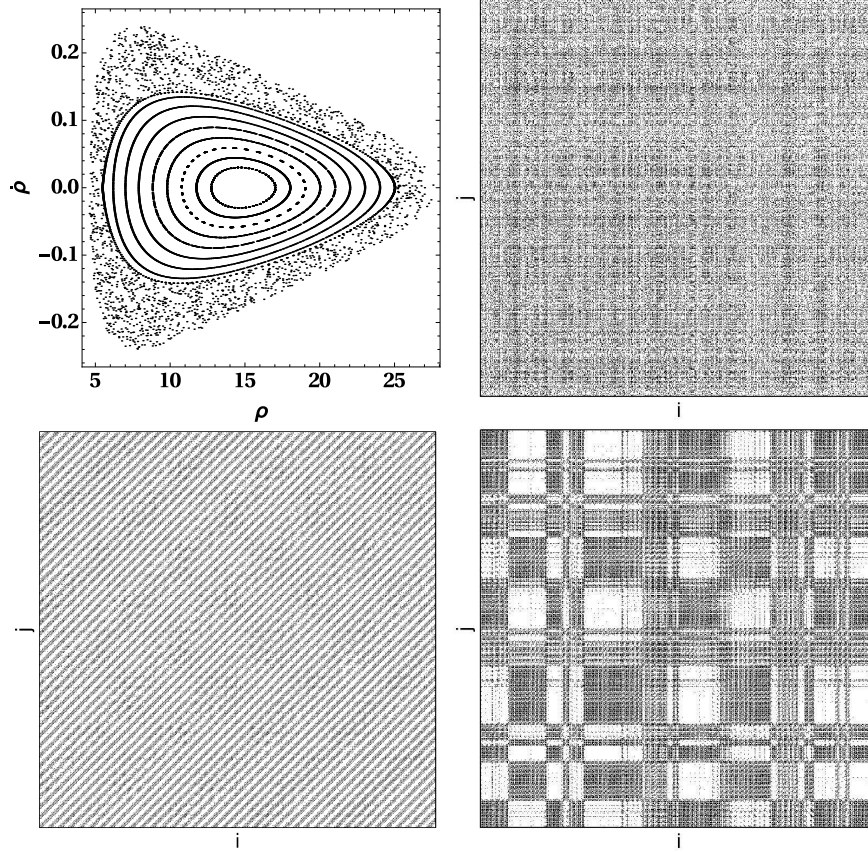


Fig. 1. The top left panel shows a Poincaré section recorded in the equatorial plane ( $z = 0$  and  $\dot{z} > 0$ ) for the set of trajectories with parameter values  $E = 0.97$ ,  $L_z = 3$ ,  $a = 0.6$ ,  $M = 1$ ,  $b = 3$ . The last three quantities define a spacetime for which the quadrupole deviation parameter reads  $q \approx 4.88 > 0$ . This implies that the corresponding compact object is more prolate than a Kerr black hole. The top right panel shows the RP of the pure noise. The bottom left is the RP of a regular orbit starting from  $\rho = 24$ ,  $\dot{\rho} = 0$  on the Poincaré section. The bottom right is the RP of a chaotic orbit starting from  $\rho = 26$ ,  $\dot{\rho} = 0$  on the Poincaré section.

RP are representing the consecutive points of the time series. In other words  $i$ ,  $j$  represent the time evolution, since  $\tau$  is equal to  $i \Delta\tau$  and  $j \Delta\tau$ , where  $\Delta\tau$  is the time step at which the data points of the time series are registered.

For individual cases a visual survey of RPs is a reliable method to discern regular from chaotic motion, and determinism from noise. Nevertheless, in order to perform a systematic analysis of the measured or simulated data it is necessary to employ a more systematic approach based on the recurrence quantification analysis (RQA). Indicators obtained by RQA provide various statistical measures of recurrences. Their definitions and basic properties can be found in the review Ref. 34. In our

8 *Georgios Lukes-Gerakopoulos, Ondřej Kopáček*

analysis, we employ the indicator measuring the overall recurrence rate

$$RR(\varepsilon) = \frac{1}{N^2} \sum_{i,j=1}^N \mathbf{R}_{ij}(\varepsilon) \quad , \quad (21)$$

which determines the relative density of recurrence points in the RP constructed from the time series of  $N$  data points, and the indicator

$$DET(\varepsilon) = \sum_{l=l_{\min}}^N lP(\varepsilon, l) \bigg/ \sum_{i,j=1}^N \mathbf{R}_{ij}(\varepsilon) \quad , \quad (22)$$

which reflects the amount of determinism present in the signal by measuring the ratio of the number of recurrence points forming diagonal lines in the RP (of the length at least  $l_{\min}$ ) to the number of all recurrence points. Function  $P(\varepsilon, l)$  represents the histogram of lengths  $l$  of the diagonal lines in the RP:

$$P(\varepsilon, l) = \sum_{i,j=1}^N (1 - \mathbf{R}_{i-1,j-1}(\varepsilon))(1 + \mathbf{R}_{i+l,j+l}(\varepsilon)) \prod_{k=0}^{l-1} \mathbf{R}_{i+k,j+k}(\varepsilon) \quad . \quad (23)$$

The above equations show that the numerical values of the RQA measures depend strongly on the value of recurrence threshold  $\varepsilon$ , which has to be taken into account in the analysis. In general,  $DET$  parameter is a reliable measure of determinism<sup>a</sup>. Recurrence analysis and RQA have already been applied to detect the onset of chaos in various non-integrable relativistic systems.<sup>13,14,36-39</sup> In these systems the RQA indicator  $DIV$  defined as an inverse value of the length of the longest diagonal line found in the RP

$$DIV = \frac{1}{\max_{i=1,\dots,N}\{l_i\}} \quad (24)$$

proved to be very useful due to its connection to Lyapunov exponents. In the present work, however, we combine the recurrence indicators  $RR$  and  $DET$  to obtain operational criterion allowing to detect the deterministic nature of (simulated) signals with noise. In Ref. 40 a similar criterion has been recently applied to discern chaos from noise in signals from X-ray binaries. Here, this criterion is tested for the first time for the trajectories with the dissipation due to the gravitational radiation reaction (Sec. 4.2).

#### 4. RQA discerning determinism from noise

Noise affects the appearance of RPs and values of RQA indicators. Nevertheless, it has been shown that proper choice of the threshold parameter  $\varepsilon$  may minimize the impact of noise and recurrence analysis remains reliable for reasonable noise levels.<sup>33,34</sup> In the following we shall investigate what is the highest noise level which

<sup>a</sup>Although in Ref. 30 it has been shown that  $DET$  may fail in some artificial non-physical systems.

might be present in the signal so that its deterministic nature is still detectable by means of recurrence analysis.

In our case, the noise is introduced by adding the function `RandomReal[-x, x]` to each component of the orbit  $\mathbf{y} = \{\rho, \dot{\rho}, z, \dot{z}\}$ . By varying  $x$  we set the level of noise we want to add to the signal. In order to study the degree of stochasticity in the signal, we define a noise-to-signal (NS) ratio as  $NS \equiv x/\mu(|y_i|)$  by taking the mean value for each component of the analyzed temporal segment of the trajectory. In fact, noise-to-signal  $NS$  is just the inverse value of the commonly used signal-to-noise ratio  $SN$ , i.e.  $NS \equiv SN^{-1}$ , but the former is more appropriate in our context, since we investigate the effect of gradually increasing noise level in simulated data.

Recurrence analysis is a robust method highly suitable for experimental data as it accepts the data in a raw state and still detects fundamental properties of underlying dynamical system which are non-trivially encoded in the signal. In the case of a gravitational wave signal from an EMRI we expect to obtain a one dimensional interferometric data series for the analysis. This series will represent the spacetime perturbation as detected by the apparatus. However, the characteristic frequencies of the trajectory of the inspiraling object are encoded in the spacetime perturbation modes  $h_+$  and  $h_\times$ . For example, the correlation between the spacetime perturbation modes and the components of the trajectory is implied in Ref. 3 and explicitly shown in Figs. 8 and 9 of Ref. 18 for  $h_+$ . Having this in mind, one can directly investigate the trajectory of the inspiral instead of the waveforms of the perturbation modes. Since the recurrent patterns of the trajectory inherently reflect frequencies of the underlying dynamical system, it is reasonable to assume that the conclusions found in Ref. 18 for standard frequency analysis tools remain valid also for the recurrence analysis, and thus, we can use the trajectory directly instead of the simulated waveforms derived from this trajectory.

We performed the analysis for each component of the trajectory separately, i.e. we treated each component as an independent one dimensional time series. Nevertheless, we also checked the case when the components are used simultaneously. We found that the analysis with such a varied data sets led to equivalent, and similarly indicative, results. This outcome was expected since the MSM spacetime does not provide separable system (unlike Kerr spacetime). Therefore, without loss of generality, we discuss here the results based on the  $\rho$  component only. Note that the analysis was performed in a reconstructed phase space as discussed in appendix Appendix A.

#### 4.1. Geodesic case

We begin with the analysis of orbits in the geodesic scenario in which the dissipation is neglected. In particular, in Fig. 2 we inspect RPs of regular trajectory (the one introduced in Fig. 1) with gradually increasing noise. We observe that diagonal patterns characteristic for regular motion are visible for the noise levels up to  $NS \approx 15\%$ . For higher noise levels the visual detection of the deterministic component of

10 *Georgios Lukes-Gerakopoulos, Ondřej Kopáček*

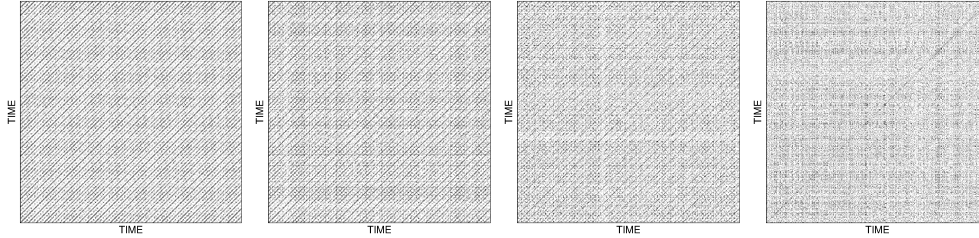


Fig. 2. A series of RPs for threshold  $\varepsilon = 1.8$  corresponding to the regular trajectory of Fig. 1 with the amount of noise increasing from left to right. The first panel has zero noise, the second has  $NS \approx 10\%$ , the third has  $NS \approx 15\%$ , and the last panel shows pure noise. We see characteristic diagonal pattern typical for regular trajectories being gradually buried in the increasing noise.

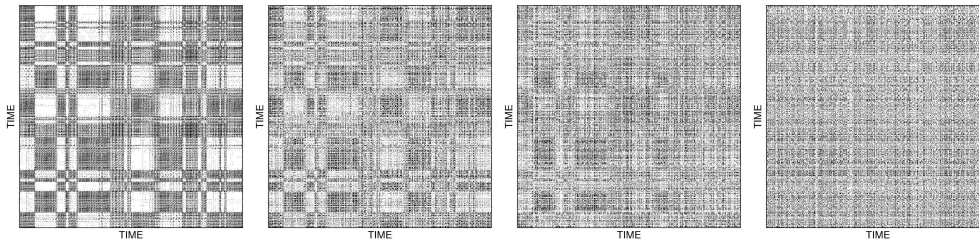


Fig. 3. A series of RPs for threshold  $\varepsilon = 2.15$  corresponding to the chaotic trajectory of Fig. 1 with the amount of noise increasing from left to right. The first panel has zero noise, the second has  $NS \approx 5\%$ , the third has  $NS \approx 40\%$ , and the last panel shows pure noise. We see the recurrence patterns typical for chaotic trajectories being gradually buried in the increasing noise.

the signal becomes ambiguous. In Fig. 3 we compare RPs of the chaotic geodesic trajectory (shown in the bottom right panel of Fig. 1) with increasing noise level. We identify recurrence patterns typical for deterministic chaos which are gradually dissolving in the noise. We may safely identify these deterministic patterns for the values of noise up to  $NS \approx 40\%$ . Thus, the visual analysis of RPs allows to detect the deterministic nature of the chaotic system, although the signal is considerably contaminated by the noise. While in some other respects the chaotic dynamics may mimic behavior of stochastic systems, here we observe the opposite: by means of visual survey of RPs the deterministic ingredient of the signal may be distinguished more easily from the stochastic noise if it is generated by chaotic (rather than regular) dynamics.

Nevertheless, for a systematic analysis we need a reliable quantitative criterion to detect determinism obscured by stochastic noise. This can be achieved by evaluating the dependence of  $RR$  and  $DET$  on the noise level for a sequence of values of recurrence threshold  $\varepsilon$ . In Fig. 4 we present the results for the chaotic trajectory. The values of  $RR$  and  $DET$  generally decrease with decreasing  $\varepsilon$ . On the other hand, the values of both the indicators also decrease with increasing noise level which is not known *a priori*. Therefore, we first need to conveniently fix  $\varepsilon$  (which is a free parameter in the analysis) so that we can use  $DET$  to efficiently detect

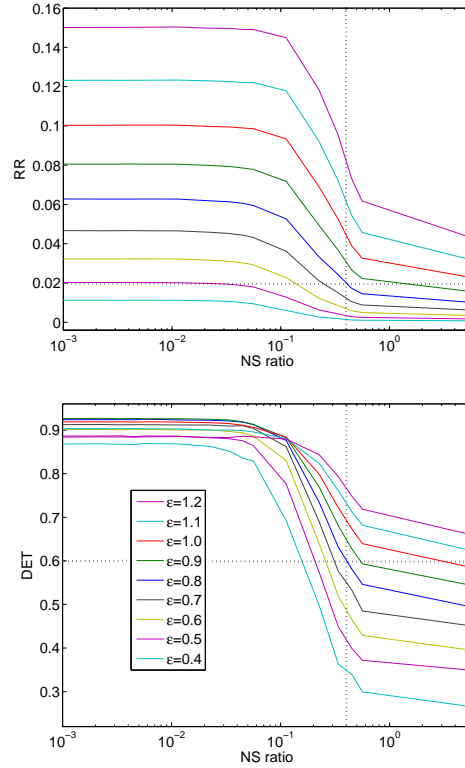


Fig. 4. The recurrence indicators  $RR$  and  $DET$  as a function of NS ratio for the chaotic trajectory. Each indicator is evaluated for several values of  $\varepsilon$  denoted in the legend of the  $DET$ -plot and corresponding also to the  $RR$ -plot. The curves for different values of  $\varepsilon$  create an ordered sequence in the both plots – lower  $\varepsilon$  gives lower recurrence rate and also lower value of  $DET$ . The asymptotic values of the indicators evaluated for the pure noise are marked on the right vertical axes by cross-marks in the corresponding colors. The critical noise level of  $NS = 40\%$  is denoted by the vertical dashed line.

determinism in the signal with generally unknown amount of noise.

We suggest the following *operational criterion*: if the value of  $DET$  is greater or equal to 0.6 for such a value of  $\varepsilon$  which gives  $RR = 0.02$ , then the signal contains deterministic component. These threshold values have been selected *ad hoc* in such a way that on the one hand we safely avoid false identification of the pure noise as deterministic, but on the other hand we maximize the noise level for which we still correctly identify the deterministic component of the signal. For the general time series containing unknown amount of noise the algorithm we propose is to tune  $\varepsilon$  to obtain  $RR = 0.02$  and check the value of  $DET$  evaluated with this  $\varepsilon$ . Applying this criterion in Fig. 4 we see that determinism in the analyzed data may be identified for the values of NS at least up to  $\approx 40\%$  before the corresponding  $DET$ -curves (i.e., those with  $\varepsilon$  which gives  $RR = 0.02$  at given noise level) start to drop below

12 *Georgios Lukes-Gerakopoulos, Ondřej Kopáček*

$DET = 0.6$ . In particular, in Fig. 4 we observe that at noise level  $NS \approx 40\%$  the condition  $RR = 0.02$  is met by the blue curve evaluated with  $\varepsilon = 0.8$  and at the same noise level the corresponding blue  $DET$ -curve just meets the boundary value of  $DET = 0.6$ . With more noise the relevant  $\varepsilon$  would lead to  $DET < 0.6$ .

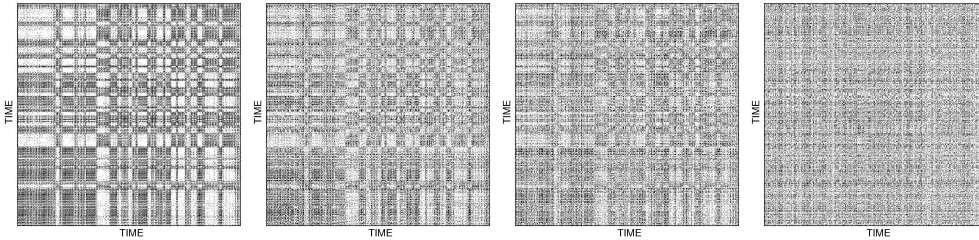


Fig. 5. A series of RPs for threshold  $\varepsilon = 2.15$  corresponding to a dissipating chaotic trajectory ( $\nu = 10^{-4}$ ) with increasing amount of noise from left to right. The first panel has zero noise, the second has  $NS \approx 3\%$ , the third has  $NS \approx 20\%$ , and the last panel shows pure noise. We see the chaotic patterns being gradually buried in the increasing noise.

#### 4.2. *Inspiraling case*

To make our investigation more realistic, we have to include the adiabatic dissipation due to the radiation reaction into our evolution scheme. To achieve this we follow the approximative approach employed in Refs. 4, 18. In this scheme, the mass ratio  $\nu = m/M$  of the EMRI adjusts the applied dissipation rate, where  $m$  is the mass of the inspiraling body. The higher  $\nu$  is, the higher the applied dissipation will be. In general, as the dissipation increases an inspiral shifts faster between geodesic orbits. Thus, by increasing the dissipation the recurrence rate is reduced, which implies that the recurrence analysis has a certain limit of applicability. The question is whether this limit is sufficient for an EMRI or not.

The upper limit of the mass ratio for an EMRI is  $\nu = 10^{-4}$ .<sup>1</sup> Thus, by checking this upper limit, we apply the highest rate of dissipation on the inspiral. Moreover, we intentionally choose the chaotic case which maximally differs from the scenarios covered by currently existing templates, since the current templates are based on the assumption of an integrable dynamical background which does not allow chaotic dynamics. By combining chaotic motion in an EMRI and the dissipation with high value of  $\nu$  we obtain the worst case scenario for the current templates and we test whether the recurrence method could be used under these circumstances. In particular, in Fig. 5 we compare RPs of chaotic dissipative trajectory with increasing amount of noise. The typical patterns of deterministic chaos are still partially visible even if the noise increases to  $NS \approx 20\%$ . Thus, the deterministic nature of the signal with high noise level may still be visually identified in RPs, even if the upper limit of mass ratio is considered. For the regular orbit with dissipation, the limit is  $NS \approx 15\%$  (we do not present the plots for this case). Thus, as in the geodesic

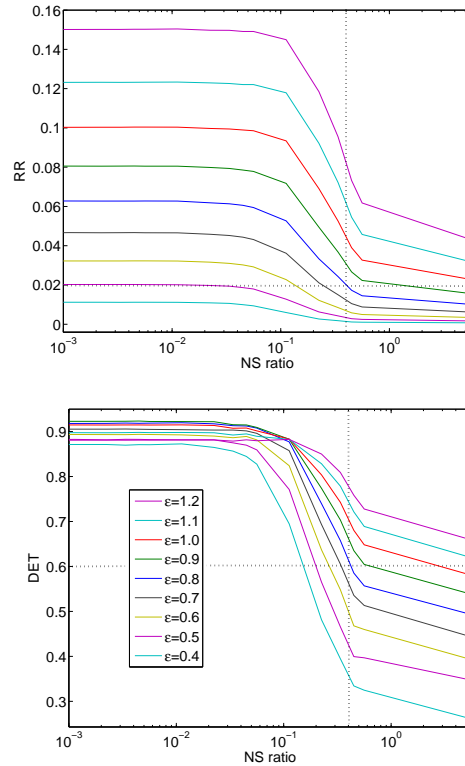


Fig. 6. The recurrence indicators  $RR$  and  $DET$  as a function of  $NS$  ratio for a dissipating chaotic trajectory. Each indicator is evaluated for several values of  $\epsilon$  denoted in the legend of the  $DET$ -plot. The critical noise level of  $NS = 40\%$  is denoted by the vertical dashed line.

case, the visual detection of determinism appears to be more effective for chaotic trajectories.

Applying our criterion on values of RQA indicators  $RR$  and  $DET$ , we find that the deterministic nature of the signal may be detected for the noise levels up to  $NS \approx 40\%$  for the chaotic trajectory with dissipation (see Fig. 6). Although the appearance of RPs and visual stability of their characteristic patterns is considerably affected by the dissipation (compare Figs. 3 and 5), the behavior of  $RR$  and  $DET$  indicators is almost indifferent to the dissipation (compare Figs. 4 and 6) and the critical noise level  $NS \approx 40\%$  is comparable to the geodesic case discussed in Sec. 4.1. Moreover, unlike in the case of visual detection of determinism using RPs, here the chaotic orbits are not privileged, i.e. the noise to signal limit is the same for chaotic and regular orbits.

Moreover, we believe that the values of the critical noise levels mentioned above are in fact the lower limits. The theoretical reliability of the method is probably considerably higher and its performance could be enhanced by further tuning.

## 5. Conclusions

We have shown that visual survey of recurrence plots allows to detect determinism in the signal with considerable amount of noise. We have formulated a quantitative criterion of determinism of the signal based on the combination of RQA indicators  $RR$  and  $DET$  which works equivalently for regular and chaotic dynamical regimes of both the conservative and the dissipative versions of the employed model approximating an EMRI. Our operational criterion allows us to discern deterministic signal from noise up to  $NS \lesssim 40\%$ , and it remains a robust method even if dissipation is considered.

Our work is a theoretical dynamical study of a chaotic system with dissipation motivated by EMRI systems. This study indicates that chaos is still relevant when dissipation and stochastic noise are taken into account. In order to explore whether the recurrent analysis can be used as a reliable supplementary tool to matched filtering during gravitational data analysis, it would require to proceed to more astrophysically relevant signals. More relevant types of noise, e.g. frequency dependent, should be employed, and the operational criterion should be further fine-tuned to increase the critical noise levels. Nevertheless, new templates for matched filtering would be necessary in order to obtain values of EMRI's physical parameters (as mass and spin), which cannot be deduced from the recurrence analysis.

## Acknowledgements

G.L.-G. and O.K. acknowledge the support from Grant No. GACR-17-06962Y. O.K. acknowledges the support from the COST CZ program of the Czech Ministry of Education (project LD15061). Discussions with Petra Suková are highly appreciated.

## Appendix A. Parameters of the recurrence analysis

Using the single component approach in the analysis, we reconstruct the phase space portrait by means of the delay embedding method based on the Takens' embedding theorems.<sup>41</sup> A crucial step is to set the embedding dimension  $\mathcal{N}$  corresponding to the dimension of the trajectory's manifold. Setting different values of  $\mathcal{N}$  in the analysis we indeed confirm that in our case the proper value leading to reliable outcome is  $\mathcal{N} = 4$  as one would expect in the non-integrable system of two degrees of freedom. Although the phase space actually has 8 dimensions, only the 4 of them (in our coordinate choice  $\{\rho, \dot{\rho}, z, \dot{z}\}$ ) are dynamically important.

To construct RPs and compute RQA indicators we use the CRP ToolBox<sup>34</sup> installed on Matlab (R2014b). The segment of the trajectory we use for the analysis is given by the range of integration parameter  $\tau$  (proper time). To obtain RPs we use  $\tau \in \langle 0, 2 \times 10^5 \rangle$  with the step-size  $\Delta\tau = 200$ , i.e., 1000 data points. For the evaluation of RQA measures we use  $\tau \in \langle 0, 4 \times 10^5 \rangle$  with  $\Delta\tau = 200$ , i.e., 2000 data points. We employ Euclidean norm (see Refs. 34, 36 for the discussion of the

choice of the norm in this context). For the recurrence analysis, the time series is normalized to have zero mean and standard deviation  $\sigma = 1$ . For the evaluation of the *DET* indicator we use the default value of the minimal length of the diagonal line  $l_{\min} = 2$ .

## References

1. P. Amaro-Seoane, S. Aoudia, S. Babak, P. Binétruy, E. Berti, A. Bohé, C. Caprini, M. Colpi, N. J. Cornish, K. Danzmann, J.-F. Dufaux, J. Gair, I. Hinder, O. Jennrich, P. Jetzer, A. Klein, R. N Lang, A. Lobo, T. Littenberg, S. T. McWilliams, G. Nelemans, A. Petiteau, E. K Porter, B. F. Schutz, A. Sesana, R. Stebbins, T. Sumner, M. Vallisneri, S. Vitale, M. Volonteri, H. Ward, B. Wardell, *GW Notes* **6** (2013) 4.
2. A. J. K. Chua and J. R. Gair, *Classical Quant. Grav.* **32** (2015) 232002.
3. K. Kiuchi and K.-I. Maeda, *Phys. Rev. D* **70** (2004) 064036.
4. G. Lukes-Gerakopoulos, T. A. Apostolatos and G. Contopoulos, *Phys. Rev. D* **81** (2010) 124005.
5. S. Suzuki and K. Maeda, *Phys. Rev. D* **55** (1997) 4848.
6. M. D. Hartl, *Phys. Rev. D* **67** (2003) 024005.
7. M. D. Hartl, *Phys. Rev. D* **67** (2003) 104023.
8. W.-B. Han, *General Relativity and Gravitation* **40** (2008) 1831.
9. P. Amaro-Seoane, P. Brem, J. Cuadra and P. J. Armitage, *Astrophys. J.* **744** (2012) L20.
10. W. M. Vieira and P. S. Letelier, *Astrophys. J.* **513** (1999) 383.
11. X. Wu and H. Zhang, *Astrophys. J.* **652** (2006) 1466.
12. O. Semerák, and P. Suková, *Mon. Not. R. Astron. Soc.* **404** (2010) 545.
13. O. Semerák, and P. Suková, *Mon. Not. R. Astron. Soc.* **425** (2012) 2455.
14. P. Suková, and O. Semerák, *Mon. Not. R. Astron. Soc.* **436** (2013) 978.
15. V. Witzany, O. Semerák, and P. Suková, *Mon. Not. R. Astron. Soc.* **451** (2015) 1770.
16. C. Bambi, *Mod. Phys. Lett. A* **26** (2011) 2453.
17. E. Guéron, and P. S. Letelier, *Phys. Rev. E* **66** (2002) 046611.
18. J. R. Gair, C. Li and I. Mandel, *Phys. Rev. D* **77** (2008) 024035.
19. W.-B. Han, *Phys. Rev. D* **77** (2008) 123007.
20. G. Contopoulos, *Order and chaos in dynamical astronomy*, (Springer, Berlin, 2002)
21. J. Laskar, *Celest. Mech. Dyn. Astron.* **56** (1993) 191.
22. V. S. Manko, J. D. Sanabria-Gómez and O. V. Manko, *Phys. Rev. D* **62** (2000) 044048.
23. F. L. Dubeibe, L. A. Pachón, and J. D. Sanabria-Gómez, *Phys. Rev. D* **75** (2007) 023008.
24. G. Lukes-Gerakopoulos, *Phys. Rev. D.* **89** (2014) 043002.
25. E. Harms, G. Lukes-Gerakopoulos, S. Bernuzzi, and A. Nagar, *Phys. Rev. D* **93** (2016) 044015; *Phys. Rev. D.* **94** (2016) 104010.
26. E. Berti and N. Stergioulas, *Mon. Not. R. Astron. S.* **350** (2004) 1416.
27. E. Berti, F. White, A. Maniopolou and M. Bruni, *Mon. Not. R. Astron. S.* **358** (2005) 923.
28. C. Skokos, *Lect. Notes Phys.* **790** (2010) 63.
29. Y. Sota, S. Suzuki, and K.-I. Maeda, *Classical Quant. Grav.* **13** (1996) 1241.
30. N. Marwan, *Int. J. Bifurcat. Chaos* **21** (2011) 1003.
31. J. P. Eckmann, K. S. Oliffson and D. Ruelle, , *Europhys. Lett.* **5** (1987) 973.
32. M. Thiel, M. Carmen Romano and J. Kurths, *Phys. Lett. A* **330** (2004) 343.
33. M. Thiel, M. Carmen Romano, J. Kurths, R. Meucci, E. Allaria and F. T. Arecchi, *Physica D* **171** (2002) 138.

16 *Georgios Lukes-Gerakopoulos, Ondřej Kopáček*

34. N. Marwan, M. Carmen Romano, M. Thiel and J. Kurths, *Phys. Rep.* **438** (2007) 237.
35. S. Schinkel, O. Dimingen and N. Marwan *Eur. Phys. J. Spec. Tops.* **164** (2008) 45-53.
36. O. Kopáček, V. Karas, J. Kovář and Z. Stuchlík, *Astrophys. J.* **722** (2010) 1240.
37. O. Kopáček, V. Karas, J. Kovář and Z. Stuchlík, *AIP Conf. Proc.* **1283** (2010) 278.
38. O. Kopáček and V. Karas, *J. Phys. Conf. Ser.* **600** (2015) 012070.
39. J. Kovář, O. Kopáček, V. Karas and Y. Kojima, *Classical Quant. Grav.* **30** (2013) 025010.
40. P. Suková, M. Grzedzielski and A. Januk, *Astron. Astrophys.* **586** (2016) 18.
41. F. Takens, *Lect. Notes Math.* **898** (1981) 366.